processes

MDPI

Article

Increasing Surface Functionalities of $FeCl_3$-Modified Reed Waste Biochar for Enhanced Nitrate Adsorption Property

Peijing Kuang [1], Yubo Cui [1,*], Zhongwei Zhang [1], Kedong Ma [1], Wanjun Zhang [1], Ke Zhao [2] and Xiaomeng Zhang [1]

[1] College of Environment and Resources, Dalian Minzu University, Dalian 116600, China; kuangpeijing@dlnu.edu.cn (P.K.)
[2] Key Laboratory of Songliao Aquatic Environment, Ministry of Education, Jilin Jianzhu University, Changchun 130118, China
* Correspondence: cyb@dlnu.edu.cn; Tel./Fax: +86-411-87656335

Abstract: Ferric chloride ($FeCl_3$) modified reed straw-based biochar was synthesized to remove nitrate from aqueous solutions and achieve waste recycling. The adsorption of nitrate onto Fe-RBC-600 adsorbents could be described by the pseudo-second-order kinetic model and fitted to Langmuir adsorption, and the maximum adsorption capacity predicted using the Langmuir model was 272.024 mg g^{-1}. The adsorbent characterization indicated that a high temperature of 600 °C and an oxygen-poor environment could develop a hydrophobic surface and O-containing functional groups on the biochar, which provided more binding sites for Fe^{3+}/Fe^{2+} attachment and increased the surface functionality of Fe-RBC-600 with iron oxide formation. The increasing surface functionality successfully enhanced the nitrate adsorption property. The mechanism of nitrate adsorption was mainly attributed to the physical adsorption onto the positive surface and sequential chemical reduction by Fe^{2+}, and the electrostatic adsorption by protonated amine groups.

Keywords: reed waste biochar; nitrate adsorption property; iron modification; surface functionalities; mechanism

Citation: Kuang, P.; Cui, Y.; Zhang, Z.; Ma, K.; Zhang, W.; Zhao, K.; Zhang, X. Increasing Surface Functionalities of $FeCl_3$-Modified Reed Waste Biochar for Enhanced Nitrate Adsorption Property. *Processes* **2023**, *11*, 1740. https://doi.org/10.3390/pr11061740

Academic Editor: Wen-Tien Tsai

Received: 21 March 2023
Revised: 10 April 2023
Accepted: 22 May 2023
Published: 7 June 2023

1. Introduction

As a kind of oxide of nitrogen, nitrate commonly exists in various types of agricultural, domestic and industrial wastewater and drinking water, and it gives rise to eutrophication and poses a serious threat to the environment [1]. Excess nitrate ingestion induces significant risk to human health, including infection diseases, such as cyanosis and cancer of the alimentary canal [2,3]. Based on this, the maximum accepted levels of nitrate concentration in drinking water are stipulated as 10 mg-N/L by the U.S. Environmental Protection Agency, 11.3 mg-N/L by the World Health Organization (WHO) and European drinking water directive and 20 mg-N/L according to China's grade III standard for groundwater quality (GB/T 14, 848-2017) [4,5]. Numerous techniques for the removal of nitrate have been reported with varying levels of efficiency, cost and ease of operation. Adsorption is generally considered a desirable technology due to its high efficiency, low energy input and simplicity of operation [6], making it effective in reducing nitrate concentrations to a permissible value. The adsorbent is at the core of the adsorption process. Biochar, produced by the thermal pyrolysis of biomass, exhibited great potential as an attractive adsorbent owing to its unique characteristics of a high specific surface area, well-developed pore structure and rich surface functionality [7]. Nitrate could be removed by attaching specific functional groups of biochar with specific interactions [8]. Meanwhile, biomass-based biochar materials placed carbon (C) into a recalcitrant form, functioning as a negative greenhouse gas emission technology with sustainable development co-benefits, also aiding in climate change mitigation [9].

As we know, many kinds of agriculture and forestry plants become waste after harvest and wilting, and these may be discarded directly or burned on the spot, resulting in envi-

ronmental pollution. Many research efforts have been dedicated to converting agriculture and forestry waste to biochar to act as the adsorbents in subsequent nitrate removal [10]. However, the negative biochar surface with oxygen functional groups had an electrostatic repulsion to anions, and resulted in a lower adsorption capacity in the range of between 16 and 65 mmol/kg for nitrate [11–13]. Research found that metal-modified biochar exhibited a higher nitrate adsorption ability based on the specific affinity of metal oxide toward nitrate, and introducing iron (hydr)oxides into porous biochar has been a widely used method for metal modification [14]. It was reported that the nitrate removal rate in groundwater treated with bagasse biochar was less than 5%, while this increased to nearly 80% after modification with nano-zero-valent iron [15]. Li et al. found that iron-modified reed biochar offered a higher adsorption capacity of 1.747 $mg \cdot g^{-1}$ for nitrate [16], for which the positively charged surface of iron-modified biochar attracted nitrate anions easily [17]. You et al. suggested that introducing iron oxides to the biochar surface promoted a chemical redox reaction between Fe^{2+} and NO_3^--N, and obtained the maximum nitrate adsorption capacity of 34.20 $mg \cdot g^{-1}$ [18]. Iron modification was highly efficient for enhancing the adsorption properties of biochar for nitrate owing to its selectivity towards nitrate oxyanions in the adsorption process [19,20].

From a mechanism point of view, the behavior of nitrate adsorption is mainly related to the surface functionality of biochar. The surface functionality of iron-modified biochar depends largely on the iron-containing functional groups formed through the affinity between the Fe^{3+}/Fe^{2+} and surface functional groups of unmodified biochar. Therefore, the functional groups of biochar play an important role in the surface functionality of iron-modified biochar and sequential nitrate adsorption behavior. It was proved that the formation of biochar functional groups varied based on pyrolysis conditions [21,22]. Researchers found that the partial-oxidation process under a higher pyrolysis temperature could decrease O-containing surface functionalities and increase the nitrogen content of functional groups that are believed to be predominant in governing the attachment of ions on carbon surfaces [23]. As another important pyrolysis condition, protective gas was also crucial to the change of the biochar pattern. Compared to the oxygen-poor environment of smoldering combustion, adding nitrogen as a protective gas could prevent the organic matter of biochar from burning, which also affected the composition of surface functional groups and their binding ability for ions [24]. Thus, pyrolysis conditions significantly affected the attachment of ions on the biochar due to their effects on the formation of surface functional groups. However, no systematic exploration was made on the effects of pyrolysis conditions on Fe^{3+}/Fe^{2+} attachment on the biochar and the formation of iron oxides during iron modification. The composition of iron-containing functional groups and their improvement of the surface functionality of iron-modified biochar need to be explored in detail. Furthermore, it remains unclear which iron-containing functional groups contributed to the enhanced nitrate removal, and the pathway of nitrate binding to these functional groups was still under debate.

To solve the above problems, reed straw waste was used as the biochar feedstock to alleviate nitrate pollution in water and achieve resource utilization of waste. In this study, different models and characterization methods were used to investigate the nitrate adsorption characteristics and mechanisms. The effects of pyrolysis conditions, including temperature and protective gas, on the composition of biochar functional groups and sequential formation of surface functionality for iron modified biochar were systematically investigated. Then, the iron-containing functional groups that could participate in the nitrate adsorption were identified, and their interactions were proposed.

2. Experimental

2.1. Chemicals

Potassium nitrate (KNO_3), ferric chloride hexahydrate ($FeCl_3 \cdot 6H_2O$) and reagents for nitrate detection were all obtained from Sinopharm Chemical Reagent Beijing Co., Ltd., Beijing, China. All reagents were used without further purification. As the average

concentration of nitrate in groundwater in some rural area of Dalian was detected as 50 mg-N/L for several years [25], the synthetic nitrate solutions utilized in our research was prepared with an initial nitrate concentration of 50 mg-N/L by dissolving KNO_3 in ultrapure water from a Symply-Lab water system (Direct-Q UV3, Millipore, Burlington, MA, USA).

2.2. Biochar Preparation and Modification

The reed straw used for preparation of biochar in the present study was collected from the constructed wetlands in Dalian. The straw was first cut into small pieces (about 2 cm) and washed with tap water to remove dirt and air-dried at room temperature for several days. Reed straw was crushed and sieved to a desired particle size (100~200 mesh) using heavy-duty cutting mill (FW-80, Shanghai Hu Yue Ming Scientific Instrument Co., Ltd., Shanghai, China), followed by washing with tap water and drying at 85 °C in an oven for later carbonization. Biomass was converted into reed straw biochar (RBC) in a muffle furnace at temperatures of 200 °C (RBC-200), 400 °C (RBC-400) and 600 °C (RBC-600) to explore the effect of pyrolysis temperature on biochar preparation. The pyrolysis processes proceeded under an oxygen-poor environment for 2 h at a heating rate of 10 °C/min. In order to analyze the impact of gas condition on biochar, RBC was prepared by bubbling N_2 into muffle furnace as protective gas at pyrolysis temperature of 600 °C (RBC-600-N). Iron-modified reed straw biochar (Fe-RBC) was prepared by soaking RBC in $FeCl_3$ solution at 30 °C for 12 h with a mass ratio (porous carbon to $FeCl_3$) of 1:5 and bath ratio of 1:20, and was then dried for 1.5 h.

2.3. Analysis

The surface morphology of the biochar samples before and after modification was determined using scanning electron microscope (SEM, JSM-6700F, Japanese Electronic, Tokyo, Japan). The surface phases were investigated with X-ray diffraction (XRD) using a Rigaku D/MAX-YA diffraction with Ni-filtered Cu Kα radiation (D8-02, Bruker, Mannheim, Germany). Fourier transform infrared spectroscopy (FTIR) (Vertex 70V, Bruker, Mannheim, Germany) was used to analysis the surface functional groups of biochar samples under different pyrolysis conditions. The elemental composition and chemical oxidation/reduction state of the RBC and Fe-RBC were determined with X-ray photoelectron spectroscopy (XPS) (ESCALAB250Xi, Thermo Fisher, Waltham, MA, USA). Nitrate concentrations were determined using the hydrazine sulfate reduction method, employing an automatic discontinuous chemical analyzer (DeChem-Tech, Hamburg, Germany). The specific surface area and total pore volume of biochar were examined using Brunauer–Emmett–Teller (BET) measurements, which were identified using the N_2 adsorption/desorption isotherm using a surface area analyzer (Quanta chrome Corporation, Boynton Beach, FL, USA) at 77 K.

2.4. Batch Adsorption Studies

2.4.1. Adsorption Kinetics

The solutions containing nitrate N of 50 mg L^{-1} were prepared from KNO_3. A total of 100 mL nitrate solution was poured into conical flasks with 0.5 g RBC and Fe-RBC to evaluate the adsorption capacity of biochar. They were sealed and agitated at 150 rpm in a thermostatic shaker at room temperature. Then, 1 mL water sample was withdrawn at preset time intervals (5, 10, 20, 40, 60 and 90 min) from solution to determine the residual nitrate concentration. The samples were filtered with 0.45 µm syringe filter before analysis. Adsorption experiments were conducted in triplicate and the mean values were reported. The amount of nitrate adsorbed per unit mass of adsorbent q_t (mg g^{-1}) was calculated using the following equation

$$q_t = \frac{(C_0 - C_t) \times V}{m} \quad (1)$$

where C_0 (mg L^{-1}) is the initial nitrate concentration; C_t (mg L^{-1}) is the nitrate concentration at time t; V (L) is the volume of nitrate solution; and m (g) is the mass of adsorbent.

Pseudo-first-order, pseudo-second-order and intra-particle diffusion kinetic models were proposed to reflect the variation tendency of nitrate concentration with time and quantitatively describe adsorption behaviors, which were expressed as

$$\text{pseudo-first-order}: \ ln(q_e - q_t) = ln(q_e) - k_1 t \quad (2)$$

where k_1 is the rate constant (min^{-1}) of pseudo-first-order model and q_e and q_t are the adsorption capacity (mg g^{-1}) at equilibrium and time t, respectively.

$$\text{pseudo-second-order}: \ \frac{t}{q_t} = \frac{1}{k_2 q_e^2} + \frac{1}{q_e}(t) \quad (3)$$

where k_2 is the rate constant of pseudo-second-order model (g (min mg)$^{-1}$) and q_t and q_e are the amount of adsorbate adsorbed at time t and at equilibrium (mg g^{-1}), respectively.

$$\text{intra-particle diffusion}: \ q_t = K_{id} t^{0.5} \quad (4)$$

where K_{id} is the penetration rate constant ((mg g^{-1}) $min^{-0.5}$), which was obtained from the slope of q_t versus $t^{0.5}$.

2.4.2. Adsorption Isotherm

A total of 0.2 g Fe-RBC adsorbent was added to a series of conical flasks containing 50 mL nitrate solution (25, 50, 75, 100 and 150 mg L^{-1}). A 1 mL sample was taken out after 90 min to detect nitrate concentration. Langmuir (Equation (5)), Langmuir–Freundlich (Equation (6)), Freundlich (Equation (7)), two-site Langmuir (Equation (8)) and Dubinin-Radushkevich (Equation (9)) models were employed to analyze adsorption equilibrium data, which can be expressed as

$$q_e = \frac{Q_{max} K_L C_e}{1 + K_L C_e} \quad (5)$$

$$q_e = \frac{Q_{max} K_{L-F} C_e^m}{1 + K_{L-F} C_e^m} \quad (6)$$

$$q_e = K_F C_e^{1/n} \quad (7)$$

$$q_e = \frac{Q_1 K_1 C_e}{1 + K_1 C_e} + \frac{Q_2 K_2 C_e}{1 + K_2 C_e} \quad (8)$$

$$q_e = Q_{max} exp(-\beta [RTln(1 + \frac{1}{C_e})]^2) \quad (9)$$

where q_e (mg g^{-1}) and C_e (mg L^{-1}) are the amount of nitrate uptake and nitrate concentration at equilibrium, respectively; Q_{max} (mg g^{-1}) is the fitting maximum adsorption capacity; K_L (L mg^{-1}) is the Langmuir constant; K_{L-F} (L mg^{-1}) is the Langmuir–Freundlich constant, K_F ((mg g^{-1}) (L $mg^{-1})^{1/n}$) is the Freundlich constant; n is an empirical parameter; m is the heterogeneity factor; K_1 (L mg^{-1}) and K_2 (L mg^{-1}) are the affinity coefficients; Q_1 (mg g^{-1}) and Q_2 (mg g^{-1}) are the corresponding maximum adsorption capacity ($Q_{max} = Q_1 + Q_2$); β is a constant related to adsorption energy (mol^2/kJ^2); R is an ideal gas constant (8.314 J/mol·K); and T is the thermodynamic temperature (K).

3. Results and Discussion

3.1. Characterization of Biochar

The textural properties and surface morphology of RBCs prepared with different pyrolysis temperatures and protective gases were characterized using the SEM. The surface textures of the raw reed straw were comparatively rough and uneven (Figure 1a). For RBC-200, there was no significant change in the surface morphology after pyrolysis because the reed straw was hardly carbonized under the relatively low pyrolysis temperature (Figure 1b). The heterogeneous and honeycomb-like structure could be observed in the biochar as the pyrolysis temperature increased (Figure 1c,d). RBC-600 had the most uniform pore structure, illustrating the better development at a higher temperature. The formation

of pores was probably due to the escape of volatile substances and the formation of channel structures during pyrolysis [26,27]. Little difference was observed on the surface morphology of RBC-600 (Figure 1d) and RBC-600-N (Figure 1e).

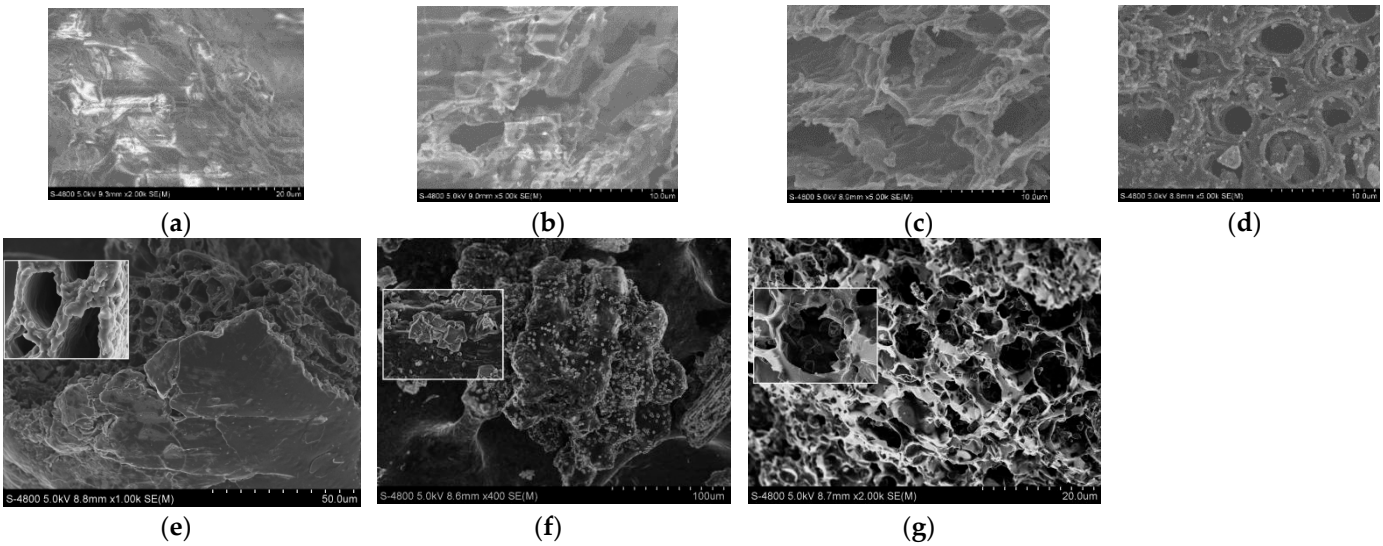

Figure 1. SEM images of the reed straw (**a**), reed straw biochar (RBC) prepared at different temperatures under oxygen-poor environment ((**b**): RBC-200, (**c**): RBC-400, (**d**): RBC-600) and 600 °C under N_2 protection (RBC-600-N) (**e**), and the surface (**f**) and pores (**g**) of iron-modified biochar (Fe-RBC-600).

The morphological characteristics of iron-modified biochar were also analyzed using SEM. After loading with $FeCl_3$, a number of small polyhedron crystals attached to the pores and surface of RBC-600 (Figure 1f,g), and made the surface of the composite rougher and less even. These results were consistent with those from other iron-modified biochar materials, which suggested that iron oxide particles could be bonded to the carbon matrix during iron modification [12]. However, the phenomenon was not observed on biochar prepared at other pyrolysis conditions. Compared to other pyrolysis temperatures, RBC-600 had abundant pores and a rugged surface and, thus, presented a good binding site for the modified materials [28]. Considering the above results, a higher temperature of 600 °C and oxygen-poor environment successfully promoted the formation of iron-modified biochar (Fe-RBC-600).

XRD patterns were used to further verify the chemical component of small polyhedron crystals formed on Fe-RBC-600 (Figure 2). The corresponding diffraction peaks could be indexed using a JCPDS (Joint Committee on Powder Diffraction Standards) X-ray powder diffraction file of No. 99–0088. The diffraction peak at 24.52° was assigned to the characteristic diffraction peaks of biochar [29], which showed no significant differences in peak intensity and angle before and after iron modification. The diffraction peaks assigned to the Fe_2O_3, Fe_3O_4, FeOOH and Fe_3C could be observed on Fe-RBC-600. $FeCl_3$ preloaded on porous carbon was proved to be hydrolyzed to $Fe(OH)_3$ and FeOOH, which could partly decompose into Fe_2O_3 [30]. Meanwhile, part of Fe_2O_3 would be reduced to FeO with reduction components [31], and FeO was converted to Fe_3C because of the interaction with reduction components [32]. It could be concluded that various iron oxides formed and adhered on the biochar surface during iron modification, improving the surface functionality of Fe-RBC-600.

Table 1 presented that the BET specific surface areas and pore size of our prepared biochar exhibited significant variations before and after modification. Compared with the surface area and average pore diameter of unmodified biochar (7.41 m^2/g, 3.806 nm), the surface area and average pore diameter decreased to 2.29 m^2/g and 1.818 nm after iron modification. The lower surface area of Fe-RBC was probably because of the abundance

of iron oxides that have a small surface area, and the decrease in the pore volume was attributed to the blockage of pores by iron oxide particles. As the radius of NO_3^- was 0.129 nm, it would be possible for nitrate to penetrate into the pores of all kinds of biochar.

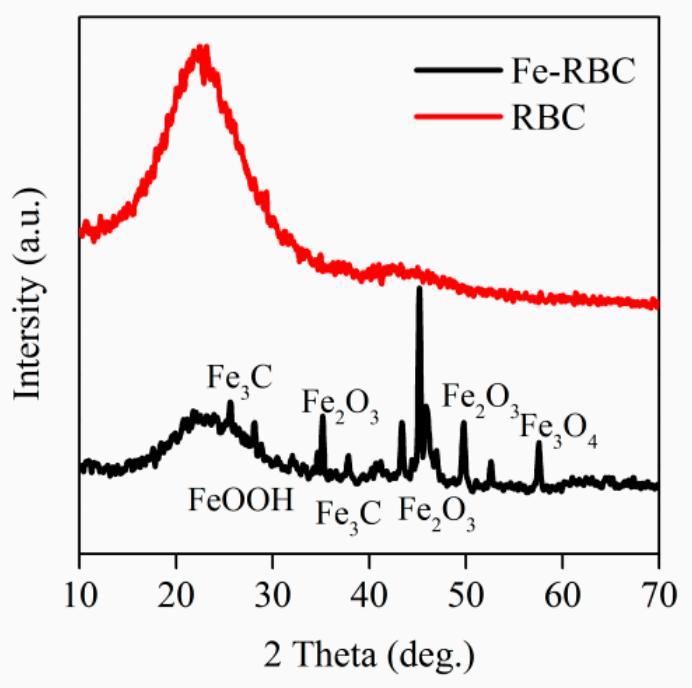

Figure 2. XRD spectra results of RBC and Fe-RBC.

Table 1. BET analysis for pore structure parameters of different kinds of modified biochar.

	RBC	Fe-RBC
Specific surface area (m^2/g)	7.412	2.289
Pore volume (cc/g)	0.011	0.003
Average pore diameter (nm)	3.806	1.818

3.2. Adsorption Kinetics and Isotherm

The nitrate adsorption capacity of RBC-600 and Fe-RBC-600 was also studied (Figure 3). A higher nitrate removal efficiency of approximately 30% could be achieved using Fe-RBC-600 after a 1.5 h operation with the adsorption capacity of 27.20 mg g^{-1} calculated using Equation (1); however, almost no nitrate was adsorbed by RBC-600. The results suggested that the iron-modified biochar provided more available activated sites for nitrate adsorption [33]. Furthermore, the Fe-RBC-600 prepared in this research had a higher adsorption capacity than some other kinds of Fe-modified materials in previous studies (Table 2). Compared with pyrolysis at 450 °C [16], a higher temperature of 600 °C can develop a better porous structure in biochar [26]. Meanwhile, the N_2 phenomenon oxygen-poor environment also promoted the formation of O-containing functional groups on biochar. These conditions provided more available activated sites for iron modification and subsequent nitrate adsorption [33]. Adel et al. [12] obtained a lower adsorption ability of biochar after iron modification, which might be because the original conocarpus waste had fewer functional groups for binding with Fe^{3+}/Fe^{2+}. The high adsorption capacity could be explained by the combination of various modification processes and, thus, there being more adsorption sites for nitrate [18,34,35]. Therefore, the iron-modified biochar prepared in our study was preferable in terms of nitrate adsorption.

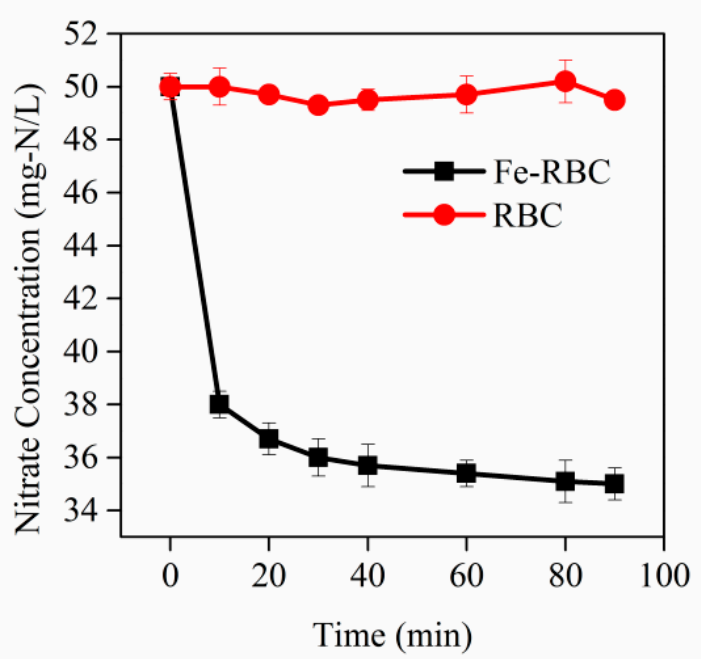

Figure 3. Variation in nitrate concentration during adsorption process using 0.5 g RBC-600 and 0.5 g Fe-RBC-600 with an initial concentration of 50 mg L^{-1} (as N).

Table 2. Comparison of NO_3^--N adsorption capacity of Fe-RBC-600 with other results.

Adsorbents	Preparation	Reactive Conditions	Adsorption Capacity (mg/g)	Reference
MgFe–LDH-modified biochar	600 °C,1 h, under N_2, 0.1 mol/L $FeCl_3$ and 0.3 mol/L $MgCl_2$	adsorbent 2.0 g/L, 24 h, initial concentration 45 mg-N/L, acid condition	7.22	[18]
HCl–Fe-modified coconut shell biochar	1.0 mol/L HCl for 2 h, 1.0 mol/L $FeCl_3$ for 6 h	adsorbent 2.0 g/L, 30 min, initial concentration 32.10 mg-N/L, initial pH 2.01	15.14	[35]
Fe–Al-modified coconut shell biochar	1.0 mol/L HCl for 1 h, 1.0 mol/L $FeCl_3$ and 1.0 mol/L $AlCl_3$ for 6	adsorbent 2.0g/L, 50 mL solution, 24 h, acid condition	34.2	[34]
FeO-modified conocarpu biochar	1 mol/L $FeCl_2$/$FeCl_3$ for 2 h, 600 °C for 4 h	adsorbent 10.0 g/L, 2 h, initial concentration 25 mg-N/L, initial pH 6	1.26	[12]
Iron-modified wheat straw biochar	450 °C, 1 mol/L $FeCl_3$	adsorbent 10.0 g/L, 2 h, initial concentration 50 mg-N/L, initial pH 6	2.47	[16]
Iron-modified reed biochar			27.20	Present study

In order to systematically investigate the behavior of nitrate adsorption onto Fe-RBC-600, different kinetic models for nitrate adsorption were analyzed (Figure 4). The residual sum of squares (RSS), chi-square analysis (χ^2) and coefficient of determination (R^2) were employed to evaluate the goodness of fit for various kinetic and isotherm models (Table 3).

As the results indicated, the pseudo-second-order model provided a better fit to the experimental data of nitrate adsorption onto Fe-RBC-600 as it had the highest R^2 value of 0.994, and the smallest RSS of 0.412 and X^2 of 0.069 compared to the results obtained from the pseudo-first-order model (R^2 = 0.883, RSS = 7.145, X^2 = 1.919). The simulated nitrate N sorption capacity of 28.51 mg g^{-1} was closer to the real value of 27.20 mg g^{-1}. This reflected

that nitrate adsorption occurred on Fe-RBC-600 as a result of chemical adsorption, and the diffusion was the rate-determining mechanism [12], which is the typical phenomenon for carbon materials modified in a similar way. Therefore, the great nitrate adsorption capacity might be attributed to the surface functionality of Fe-RBC-600, with various iron oxides adhering to promote nitrate adsorption.

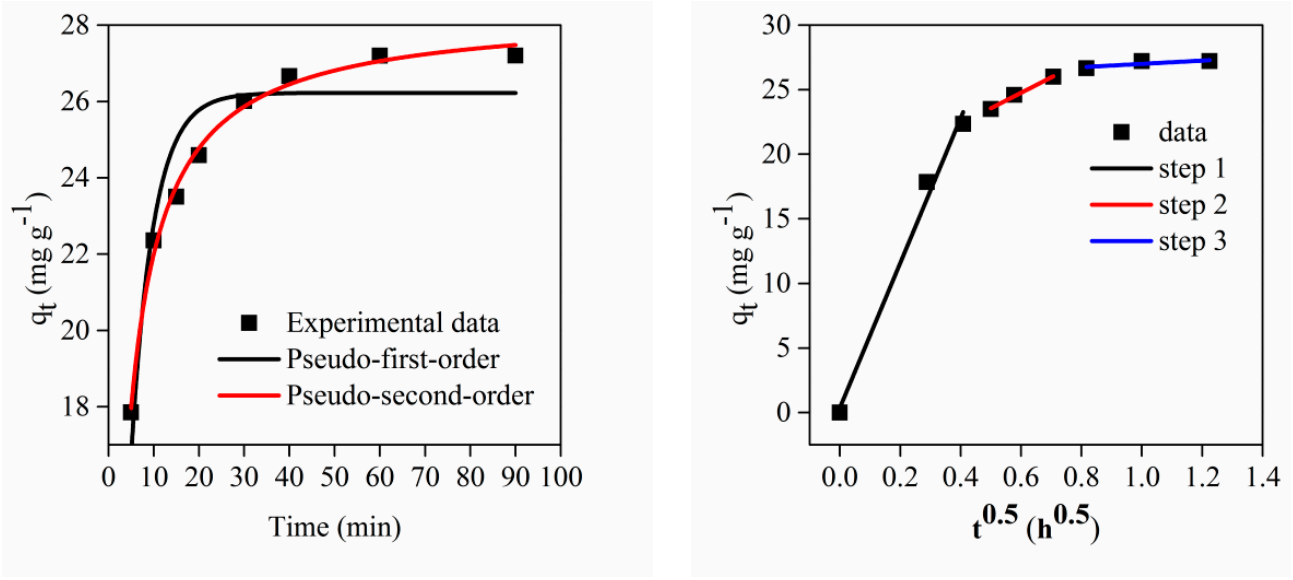

Figure 4. Kinetics for nitrate adsorption on Fe-RBC-600 composite: (**a**) pseudo-first-order and pseudo-second-order models, (**b**) intra-particle diffusion model.

Table 3. Kinetic parameters obtained from nitrate adsorption on Fe-RBC-600.

Model	C_0 (mg/L)	q_{exp} (mg g^{-1})	q_{cal} (mg g^{-1})	k_1	R^2	X^2	RSS		
pseudo-first order	50	27.22	26.22	0.203	0.883	1.191	7.145		
pseudo-second order	50	27.22	28.36	0.012	0.994	0.069	0.412		
intra-particle diffusion	k_{d1} (mg/h$^{1/2}$/g)	C_1	$R_1{}^2$	k_{d2} (mg/h$^{1/2}$/g)	C_2	$R_2{}^2$	k_{d3} (mg/h$^{1/2}$/g)	C_3	$R_3{}^2$
	56.062	0.377	0.98	11.969	17.580	0.99	1.274	25.728	0.40

Meanwhile, nitrate adsorption was also evaluated using the intra-particle diffusion model to predict whether the intra-particle diffusion was a rate-determining step. As Figure 4b shows, the graph of q_e and $t^{0.5}$ was divided into three straight lines, which indicated that the intra-particle diffusion was not the only rate-controlling step. These three regions corresponded with the external mass transfer stage, intra-particle diffusion stage and adsorption equilibrium stage during the nitrate adsorption process [36]. As adsorption theory illustrated, the initial step represented the nitrate ion's migration from solution to the surface of biochar adsorbents. The largest value of k_{d1} (56.062 mg/h$^{1/2}$/g) indicated the highest rate of nitrate removal in this stage, which might have been because of the excellent surface functionality of Fe-RBC-600, which initially provided a large amount of adsorption sites for nitrate and the solute concentration gradient was high. The second step referred to nitrate ion diffusion to the binding sites through its pore region, and the smaller value of k_{d2} (11.969 mg/h$^{1/2}$/g) might have resulted from the gradually increasing occupation of reactive sites on the adsorbent and the reducing concentration of nitrate in the solution. The smallest value of k_{d3} (1.274 mg/h$^{1/2}$/g) suggested that the nitrate adsorption process had reached the adsorption equilibrium and exhibited a slower adsorption rate.

The equilibrium adsorption isotherm is also a very important tool for designing sorption systems [37]. Figure 5 intuitively describes whether the fitted curve was close to the experimental data points for the five isotherm models. Comparatively, the best fitted model for Fe-RBC-600 was the Langmuir model, whose correlation coefficient was 0.975 (as Table 4 shows), indicating a monolayer and homogeneous/uniform adsorption process.

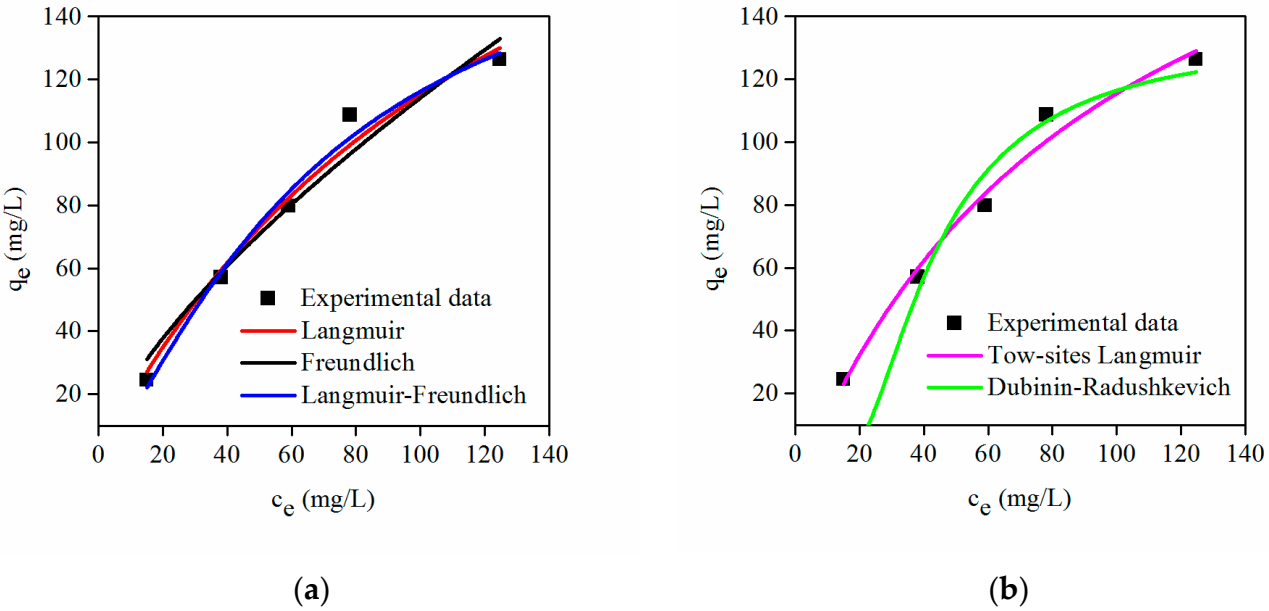

Figure 5. Adsorption isotherm for nitrate adsorption on Fe−RBC (**a**,**b**).

Table 4. Parameters of adsorption isotherm models for Fe-RBC.

Model	RSS	χ^2	R^2	Parameters
Langmuir	121.962	40.654	0.975	q = 272.024 mg g^{-1} K_L = 0.00734
Freundlich	239.528	79.843	0.951	K_F = 4.79301 n = 1.45247
Langmuir–Freundlich	84.179	42.090	0.974	q = 185.806 mg g^{-1} K_{L-F} = 0.00367 m = 1.32876
Two-site Langmuir	99.611	99.611	0.939	q_1 = 246.343 mg g^{-1} K_1 = 0.01048 q_2 = −10.546 mg g^{-1} K_2 = 1.0305 × 10^{-5}
Dubinin–Radushkevich	727.508	242.503	0.852	q_m = 133.734 mg g^{-1} β = 2.22 × 10^{-4} mol^2/kJ^2

The essential characteristics of the Langmuir isotherm were expressed in terms of a dimensionless equilibrium parameter (R_L) that was defined using the following equation:

$$R_L = \frac{1}{1 + K_L C_0} \quad (10)$$

It was proved that if the average of the R_L values for each of the different initial concentrations used was between 0 and 1, positive adsorption would occur [38]. According to the data in Table 4, the R_L values changed from 0.48 to 0.84, indicating that nitrate was adsorbed favorably with Fe-RBC-600. Meanwhile, the Freundlich constant n of 1.45247 also proved the easy occurrence of nitrate adsorption, because the values of $1/n$ were less than unity [39]. Compared to the negligible adsorption capacity of RBC-600, the maximum sorption capacity of 272.024 mg g^{-1} for Fe-RBC-600 means it could be postulated that

the attachment of iron oxides onto the biochar surface successfully increased the surface functionality and sequentially promoted the nitrate adsorption process.

3.3. Identification of Mechanism

3.3.1. FTIR Spectroscopy

The variations in functional groups on original reed straw and biochar prepared with different temperatures and protective gas were investigated using FTIR spectra. As shown in Figure 6a, the adsorption peaks at approximately 1049, 1553, 1630, 2952 and 3450 cm^{-1} for biochar prepared under different conditions could be assigned to C–OH, N–H bending of primary amines, C=O stretching of hemicellulose, C–H stretching and O–H stretching of the hydroxyl group, respectively [40]. The similar functional groups in both the original reed straw and RBC-200 also proved the unchanged chemical component of the biomass. This might have been because the lower temperature could not achieve the carbonization of biomass. As the pyrolysis temperature increased, the peak area of N–H, C=O, $–CH_2–$ and O–H stretching and bending vibrations decreased. The results revealed that the number of these groups on the biochar surface reduced during carbonization under the higher temperature, which resulted in poorer hydrophilic properties [41]. Therefore, the hydrophobic surface inhibited the adherence of water molecules and sequentially provided more binding sites for ferric ion during iron modification. Meanwhile, the oxygen atoms of acidic functional groups were proved to have intriguing interactions with a spectrum of cationic substances and increase the cation exchange capacity [42], and, thus, the existence of C=O, C–OH and O–H in RBC-600 was in favor of ferric ion attachment on the surface.

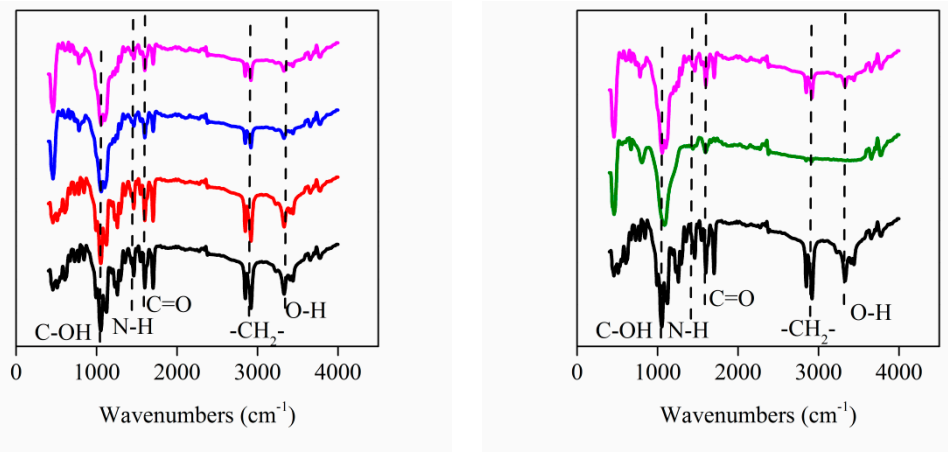

Figure 6. FTIR spectra of original reed straw biomass and RBC prepared under different pyrolysis temperatures (**a**) and gas conditions (**b**). The components are shown as follows: (1) original reed straw biomass (black), (2) RBC-200 (red), (3) RBC-400 (blue), (4) RBC-600 (pink) and (5) RBC-600-N (green).

On the other hand, the protective gas also had an effect on the surface functional groups' formation. Compared to the oxygen-poor environment, the absorbance peaks of N–H, C=O, $–CH_2–$ and O–H almost disappeared after pyrolysis under N_2 protection (Figure 6b). This was consistent with a previous report that the surface oxidation of biochar happened during aerobic thermal treatment, and the attachment of oxygen species mostly came from the gas phase [43]. Therefore, the N_2 environment hindered the formation of O-containing functional groups for biochar, and, thus, decreased the number of attachment sites for iron ions. This could explain why iron oxides could not be observed on the surface of RBC-600-N after modification. In conclusion, pyrolysis conditions of a higher temperature and oxygen-poor environment efficiently promoted the attachment of Fe^{3+}/Fe^{2+} onto RBC during iron modification.

3.3.2. XPS

XPS analysis was carried out to analyze the variation in functional groups for RBC-600 and Fe-RBC-600, which also determined the adsorption mechanism. For different kinds of biochar, C 1s spectra were deconvoluted into four peaks at 284.6, 285.2, 286.7 and 289.2 eV, which could be assigned to C–C, C–OH, C=O and COOH, respectively (Figure 7) [44]. The relative abundance of the components for RBC-600 before and after iron modification are summarized in Table 5. The C 1s spectra analysis showed that the content of the C–OH group in biochar decreased from 31.5 to 30.8% after iron modification; in contrast, the content of the C=O group increased from 10.1% to 11.2%. This suggested that the C–OH group was involved in the modification process, for which C–OH might be converted to a C=O group, accompanied by the reduction of Fe^{3+} into Fe^{2+}, which could be interpreted with the following reactions:

$$C–OH + Fe^{3+} \rightarrow Fe^{2+} + C=O \quad (11)$$

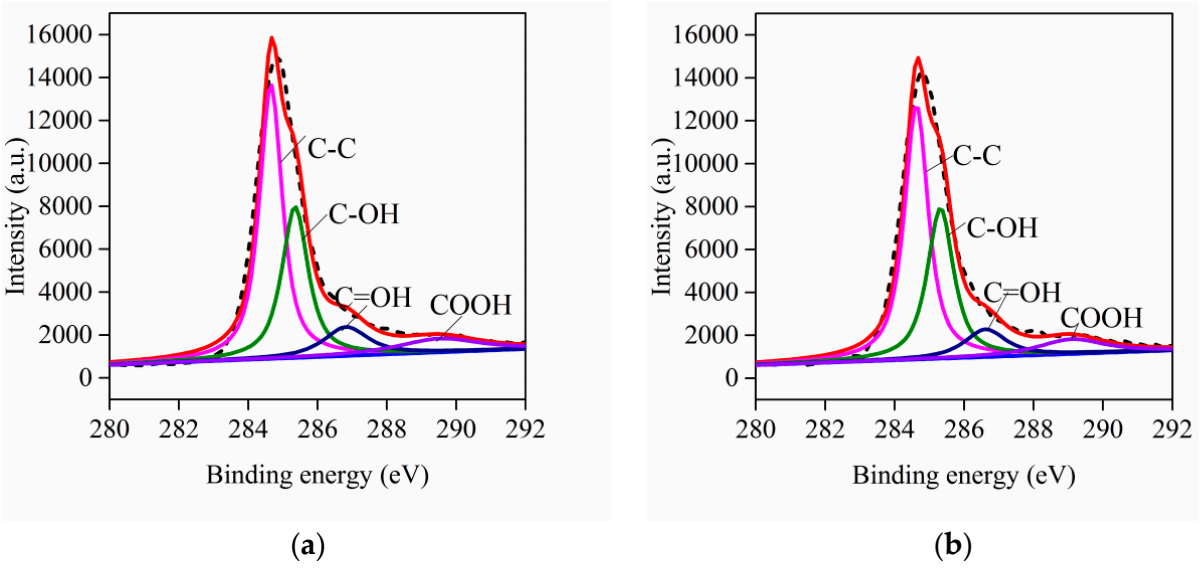

Figure 7. Deconvoluted C 1s spectra for RBC-600 (**a**) and Fe-RBC-600 (**b**).

Table 5. Relative abundance of the components from the deconvoluted C 1s spectra for RBC-600 and Fe-RBC-600.

	Relative Abundance of the Components (%)			
	C–C	**C–OH**	**C=O**	**COOH**
RBC	49.6	31.5	10.1	8.8
Fe-RBC	50.1	30.8	11.2	7.9

Meanwhile, the content of COOH decreased from 8.8% to 7.9% after iron modification, probably due to the covalent bond of iron by deprotonated carboxyl groups and iron-carboxyl band formation during modification [45]. Therefore, iron modification could be achieved in RBC-600 owing to the existence of the O-containing functional groups that served as iron-binding sites to promote the formation of various kind of iron oxides, and, thus, increased the surface functionality of Fe-RBC-600.

Meanwhile, XPS spectra were also employed to analyze the chemical composition and status of Fe-RBC-600 before and after nitrate adsorption and to explore the pathway of nitrate removal (Figure 8). The peak positions of the iron element for Fe-RBC emerged at 709.6 eV, 711 eV and 723.8 eV, 714.3 eV and 728.2 eV, corresponding to Fe^{2+}, Fe-O of O-Fe-OH, and Fe(III) of Fe_2O_3, respectively [46,47]. This allowed us to conclude that FeOOH and Fe_2O_3 were the most dominant forms of iron oxide covered on the surface of

Fe-RBC-600. FeOOH might have been formed through the interaction of chloride ions with the surface of the hydrous ion in ferric chloride solutions [48]. The existence of Fe^{2+} could be explained by the reduction of Fe(III) to Fe(II) that occurred with the oxidation of amino groups and the conversion of C–OH into C=O during iron modification [49]. Therefore, the positive surface of Fe-RBC-600 with a large amount of Fe^{3+} and Fe^{2+} could adsorb nitrate anions at the surface through electrostatic attraction. As Table 6 shows, the content of Fe^{2+} significantly decreased from 25.7% to 12.2% after nitrate adsorption, while FeOOH and Fe_2O_3 increased from 36.0% and 38.3% to 42.0% and 45.8%, respectively. This might be explained by the occurrence of a reaction between Fe^{2+} and NO_3-N, for which Fe^{2+} might have served as an electron donor between the Fe-RBC-600 surface and nitrate to accelerate nitrate reduction.

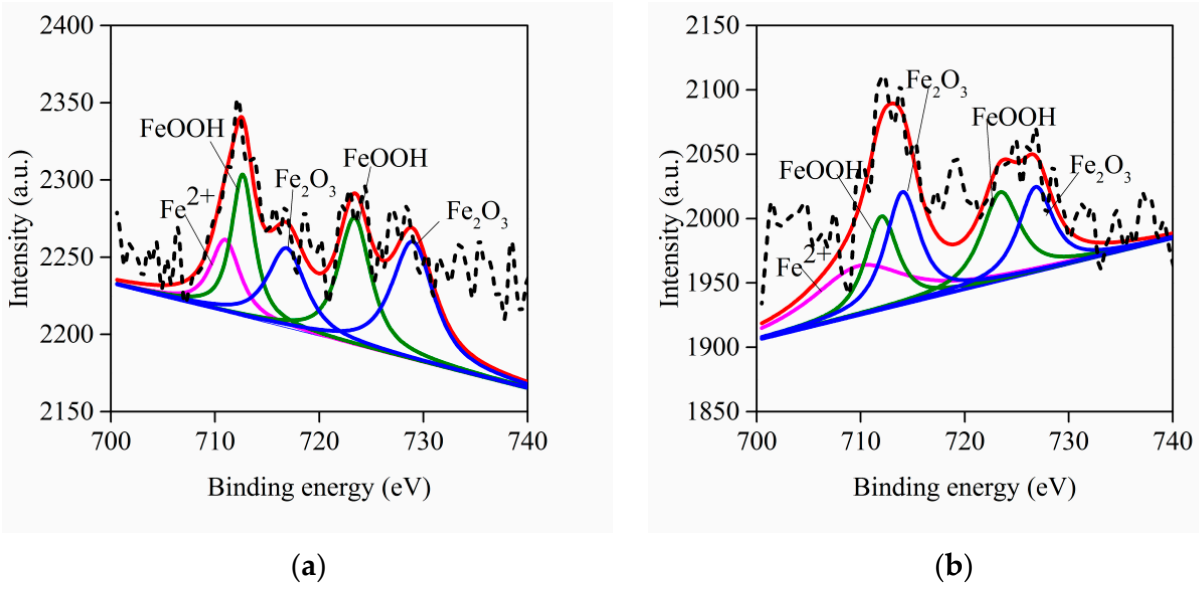

Figure 8. Fe2p XPS spectra of Fe-RBC-600 composite before (**a**) and after (**b**) nitrate adsorption.

Table 6. Relative abundance of the components from the deconvoluted Fe2p spectra for Fe-RBC-600 before and after nitrate adsorption.

	Relative Abundance of the Components (%)		
	Fe^{2+}	FeOOH	Fe_2O_3
Fe-RBC-600	25.7	36.0	38.3
nitrate-Fe-RBC-600	12.2	42.0	45.8

The N 1s horizontal spectra before and after nitrate adsorption were also analyzed. The main peak of N 1s with a binding energy could be decomposed into three distinct peaks at 399.10, 400.39 and 401.69 eV, which were quinone imine (–N=C), benzene amine ($–NH_2$ or –NH) and protonated amine ($–NH_3^+$ or $–NH_2^+$), respectively (Figure 9) [50]. After adsorbing nitrate, the existence of a new peak at 408.6 eV was confirmed as the existence of NO_3^- (Figure 9b) [51]. As Table 7 shows, the percentage of positively charged nitrogen atoms ($–NH_3^+$ or $–NH_2^+$) in the composite after adsorption of NO_3^- had decreased from 0.16% to 0.01%, indicating that the protonated amine also played a main role in nitrate removal. This might be attributable to the electrostatic attraction between the functional groups of Fe-RBC-600 and nitrate [51].

Table 7. Relative abundance of the components from the deconvoluted N 1s spectra for Fe-RBC-600 before and after nitrate adsorption.

	Relative Abundance of the Components (%)			
	–N=C	**–NH_2/–NH**	**–NH_3^+/–NH_2^+**	**NO_3^-**
Fe-RBC-600	20.8	48.3	30.8	0
nitrate-Fe-RBC-600	14.6	39.5	27.3	18.5

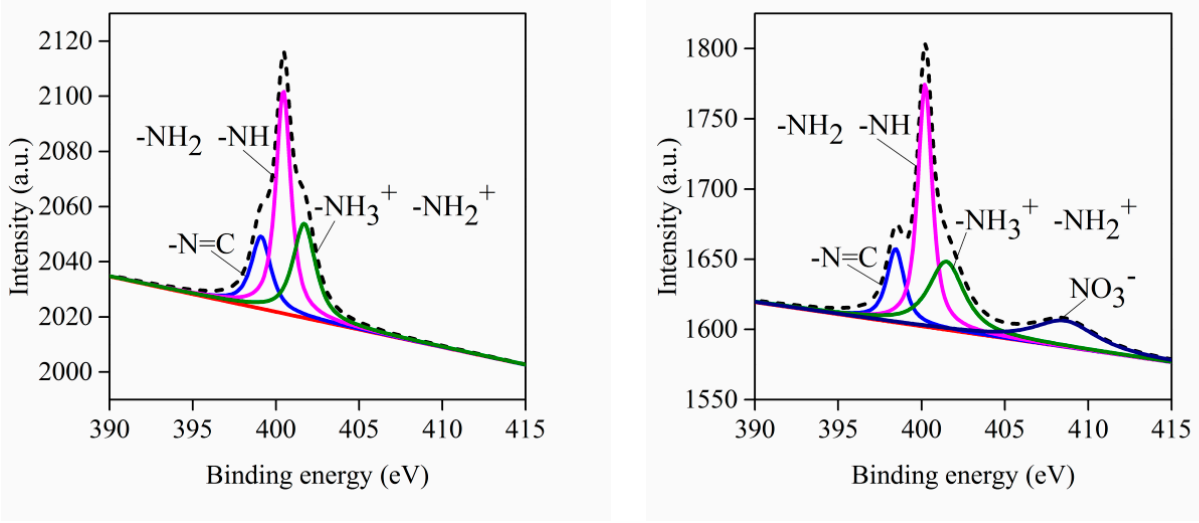

Figure 9. N 1s XPS spectra of Fe−RBC−600 composite before (**a**) and after (**b**) nitrate adsorption.

3.3.3. Adsorption Mechanisms

The proposed adsorption mechanism is indicated in Figure 10. As shown in this schematic, the hydrophobic surface and O-containing functional groups for RBC-600 could be formed under the pyrolysis conditions of a higher temperature and oxygen-poor environment, which provided binding sites for Fe^{3+}/Fe^{2+} attachment and reduction. The formation of iron oxides increased the surface functionality of Fe-RBC-600 for nitrate adsorption. Then, physical adsorption occurred between the nitrate ions and positive surface of Fe-RBC-600, for which Fe^{3+}/Fe^{2+} and protonated amine (–NH_3^+ or –NH_2^+) adsorbed nitrate through electrostatic forces. Meanwhile, the reaction between Fe^{2+} and NO_3–N also proceeded and played an important role in the nitrate adsorption process. It could be concluded that nitrate adsorbed to Fe-RBC-600 through the coordination reaction, including electrostatic attraction and chemical reduction, which occurred among the biochar, iron element and nitrate.

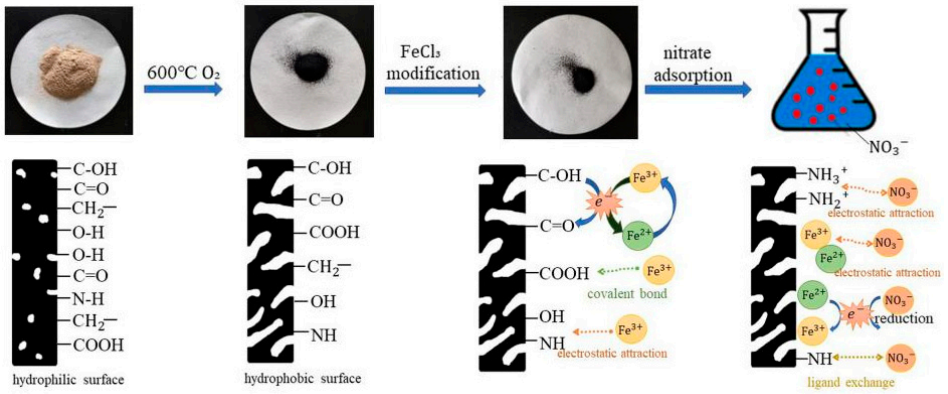

Figure 10. Mechanism of Fe-RBC-600 formation and nitrate adsorption process.

4. Conclusions

In this study, Fe-RBC-600 was successfully synthesized as an adsorbent for the effective removal of nitrate from aqueous solutions. Kinetic studies demonstrated that the adsorption of nitrate on Fe-RBC-600 was in good consistency with the pseudo-second-order kinetic model, indicating that chemisorption dominated the control step. The Langmuir isotherm model was more suitable than the Freundlich model to fit the adsorption behavior of Fe-RBC-600, and the Q_{max} value for nitrate adsorption was 272.024 mg g^{-1}. The FTIR and XPS analyses of the mechanism indicated that a higher temperature and oxygen-poor environment promoted the formation of a hydrophobic surface and O-containing functional groups on biochar, which provided a large amount of binding sites for Fe^{3+}/Fe^{2+} attachment and, thus, increased the surface functionality of Fe-RBC-600. The iron oxides embedded in the biochar exhibited a strong correlation with the enhanced nitrate adsorption property. Nitrate anions could be physically adsorbed onto the positively charged surface of Fe-RBC-600 in parallel with chemical reduction using Fe^{2+}. Meanwhile, an electrostatic attraction between protonated amine groups ($–NH_3^+/–NH_2^+$) and nitrate anions also occurred during the nitrate adsorption process. Studies towards investigating the pyrolysis conditions for increasing surface functionality have great potential to enhance the adsorption property of Fe-RBC-600 for nitrate.

Author Contributions: P.K.: conceptualization, methodology, validation, investigation, formal analysis writing—original draft, writing—review and editing; Y.C.: writing—review and editing, conceptualization, methodology, validation, supervision, funding acquisition; Z.Z.: methodology, validation, investigation; K.M.: supervision; W.Z.: project administration; K.Z.: methodology; X.Z.: writing—original draft. All authors have read and agreed to the published version of the manuscript.

Funding: This research was funded by the National Natural Science Foundation of China (No. 52270150) and the National Natural Science Foundation (Youth) of China (No. 41402208).

Institutional Review Board Statement: Not applicable.

Informed Consent Statement: Not applicable.

Data Availability Statement: All data generated or analyzed during this study are included in this published article.

Conflicts of Interest: The authors declare no conflict of interest.

References

1. Hwang, Y.H.; Kim, D.G.; Shin, H.S. Mechanism study of nitrate reduction by nano zero valent iron. *J. Hazard. Mater.* **2011**, *185*, 1513–1521. [CrossRef] [PubMed]
2. Shi, J.L.; Yi, S.N.; He, H.L.; Long, C.; Li, A.M. Preparation of nanoscale zero-valent iron supported on chelating resin with nitrogen donor atoms for simultaneous reduction of Pb^{2+} and NO^{-3}. *Chem. Eng. J.* **2013**, *230*, 166–171. [CrossRef]
3. Majumdar, D.; Gupta, N. Nitrate pollution of groundwater and associated human health disorders. *Indian J. Environ. Health* **2000**, *42*, 28–39.
4. US EPA, Region 5, Office of the Regional Administrator. *TEACH Chemical Summaries—Toxicity and Exposure Assessment for Children's Health*; EPA: Washington, DC, USA, 2007.
5. WHO. *Guidelines for Drinking-Water Quality, Incorporating Frst and Second Addenda, Recommendations*, 3rd ed.; World Health Organization: Geneva, Switzerland, 2008; Volume 1.
6. Kapoor, A.; Viraraghavan, T. Nitrate removal from drinking water—Review. *J. Envron. Eng.-Asce* **1997**, *123*, 371–380. [CrossRef]
7. Ahmad, M.; Rajapaksha, A.U.; Lim, J.E.; Zhang, M.; Bolan, N.; Mohan, D.; Vithanage, M.; Lee, S.S.; Ok, Y.S. Biochar as a sorbent for contaminant management in soil and water: A review. *Chemosphere* **2014**, *99*, 19–33. [CrossRef] [PubMed]
8. Bhatnagar, A.; Sillanpaab, M. A review of emerging adsorbents for nitrate removal from water. *Chem. Eng. J.* **2011**, *168*, 493–504. [CrossRef]
9. Monlau, F.; Sambusiti, C.; Ficara, E.; Aboulkas, A.; Barakat, A.; Carrère, H. New opportunities for agricultural digestate valorization: Current situation and perspectives. *Energy Environ. Sci.* **2015**, *8*, 2600–2621. [CrossRef]
10. Roberts, K.G.; Gloy, B.A.; Joseph, S.; Scott, N.R.; Lehmann, J. Life Cycle Assessment of Biochar Systems: Estimating the Energetic, Economic, and Climate Change Potential. *Environ. Sci. Technol.* **2010**, *44*, 827–833. [CrossRef]
11. Lehmann, J. Bio-energy in the black. *Front. Ecol. Environ.* **2007**, *5*, 381–387. [CrossRef]

12. Usman, A.R.A.; Ahmad, M.; El-Mahrouky, M.E.; Al-Omran, A.; Ok, Y.S.; Sallam, A.S.; El-Naggar, A.H.; Al-Wabel, M.I. Chemically modified biochar produced from conocarpus waste increases NO_3 removal from aqueous solutions. *Environ. Geochem. Health* **2016**, *38*, 511–521. [CrossRef]
13. Chintala, R.; Mollinedo, J.; Schumacher, T.E.; Papiernik, S.K.; Malo, D.D.; Clay, D.E.; Kumar, S.; Gulbrandson, D.W. Nitrate sorption and desorption in biochars from fast pyrolysis. *Microporous Mesoporous Mater.* **2013**, *179*, 250–257. [CrossRef]
14. Rajapaksha, U.; Chen, S.S.; Tsang, D.C.W.; Zhang, M.; Vithanage, M.; Mandal, S.; Gao, B.; Bolan, N.S.; Ok, Y.S. Engineered/designer biochar for contaminant removal/immobilization from soil and water: Potential and implication of biochar modification. *Chemosphere* **2016**, *148*, 276–291. [CrossRef] [PubMed]
15. Hafshejani, L.D.; Hooshmand, A.; Naseri, A.A.; Mohammadi, A.S.; Abbasi, F.; Bhatnagar, A. Removal of nitrate from aqueous solution by modified sugarcane bagasse biochar. *Ecol. Eng.* **2016**, *95*, 101–111. [CrossRef]
16. Li, S.; Wang, C.; He, X.; Ren, L.; Guo, Q.; Yang, L. Adsorption Characteristics of Low Concentration Nitrate-Nitrogen Onto Modified Macrophytes Biochar. *J. Ecol. Rural Environ.* **2018**, *34*, 356–362.
17. Long, L.; Xue, Y.; Hu, X.; Zhu, Y. Study on the influence of surface potential on the nitrate adsorption capacity of metal modified biochar. *Environ. Sci. Pollut. Res.* **2019**, *26*, 3065–3074. [CrossRef] [PubMed]
18. You, H.; Li, W.; Zhang, Y.; Meng, Z.; Shang, Z.; Feng, X.; Ma, Y.; Lu, J.; Li, M.; Niu, X. Enhanced removal of NO_3-N from water using Fe-Al modified biochar: Behavior and mechanism. *Water Sci. Technol.* **2019**, *80*, 2003–2012. [CrossRef]
19. Wang, Z.H.; Guo, H.Y.; Shen, F.; Yang, G.; Zhang, Y.Z.; Zeng, Y.M.; Wang, L.L.; Xiao, H.; Deng, S.H. Biochar produced from oak sawdust by Lanthanum (La)-involved pyrolysis for adsorption of ammonium (NH^{4+}), nitrate (NO^{3-}), and phosphate (PO^{43-}). *Chemosphere* **2015**, *119*, 646–653. [CrossRef]
20. Zhang, M.; Gao, B.; Yao, Y.; Xue, Y.; Inyang, M. Synthesis of porous MgO-biochar nanocomposites for removal of phosphate and nitrate from aqueous solutions. *Chem. Eng. J.* **2012**, *210*, 26–32. [CrossRef]
21. Angin, D. Effect of pyrolysis temperature and heating rate on biochar obtained from pyrolysis of safflflower seed press cake. *Bioresour. Technol.* **2013**, *128*, 593–597. [CrossRef]
22. Hou, J.; Huang, L.; Yang, Z.; Zhao, Y.; Deng, C.; Chen, Y.; Li, X. Adsorption of ammonium on biochar prepared from giant reed. *Environ. Sci. Pollut. Res.* **2016**, *23*, 19107–19115. [CrossRef]
23. Zheng, H.; Wang, Z.; Deng, X.; Zhao, J.; Luo, Y.; Novak, J.; Herbert, S.; Xing, B. Characteristics and nutrient values of biochars produced from giant reed at different temperatures. *Bioresour. Technol.* **2013**, *130*, 463–471. [CrossRef] [PubMed]
24. Liu, G.; Xu, Q.; Dong, X.; Yang, J.; Pile, L.S.; Wang, G.G.; Wang, F. Effect of Protective Gas and Pyrolysis Temperature on the Biochar Produced from Three Plants of Gramineae: Physical and Chemical Characterization. *Waste Biomass Valor.* **2016**, *7*, 1469–1480. [CrossRef]
25. Xu, Z.J.; Guo, Q.; He, Z.L. Current situation of nitrate pollution in ground water in rural area of Dalian City from 2009–2013. *Occup. Health* **2015**, *31*, 860–861.
26. Ahmad, M.; Lee, S.S.; Dou, X.; Mohan, D.; Sung, J.K.; Yang, J.E.; Ok, Y.S. Effects of pyrolysis temperature on soybean stover- and peanut shell-derived biochar properties and TCE adsorption in water. *Bioresour. Technol.* **2012**, *118*, 536–544. [CrossRef]
27. Chen, Z.; Chen, B.; Zhou, D.; Chen, W. Bisolute sorption and thermodynamic behaviour of organic pollutants to biomass-derived biochars at two pyrolytic temperatures. *Environ. Sci. Technol.* **2012**, *46*, 12476–12483. [CrossRef]
28. Shen, Y.; Chen, N.; Feng, Z.; Feng, C.; Deng, Y. Treatment of nitrate containing wastewater by adsorption process using polypyrrole-modified plastic-carbon: Characteristic and mechanism. *Chemosphere* **2022**, *297*, 134107. [CrossRef] [PubMed]
29. Sun, K.; Leng, C.Y.; Jiang, J.C.; Bu, Q.; Lin, G.F.; Lu, X.C.; Zhu, G.Z. Microporous activated carbons from coconut shells produced by self-activation using the pyrolysis gases produced from them, that have an excellent electric double layer performance. *New Carbon Mater.* **2017**, *32*, 451–459. [CrossRef]
30. Hou, T.; Sun, X.; Xie, D.; Wang, M.; Fan, A.; Chen, Y.; Cai, S.; Zheng, C.; Hu, W. Mesoporous Graphitic Carbon-Encapsulated Fe_2O_3 Nanocomposite as High-Rate Anode Material for Sodium-Ion Batteries. *Chem. A Eur. J.* **2018**, *24*, 14786–14793. [CrossRef]
31. Du, C.; Li, L.; Zhao, J.; Zhang, L.; Gao, J.; Sheng, Y.; Chen, J.; Zeng, G. Promotional removal of HCHO from simulated flue gas over Mn-Fe oxides modified activated coke. *Appl. Catal. B Environ.* **2018**, *232*, 37–48. [CrossRef]
32. Cho, D.W.; Yoon, K.; Kwon, E.E.; Biswas, J.K.; Song, H. Fabrication of magnetic biochar as a treatment medium for As(V) via pyrolysis of $FeCl_3$ -pretreated spent coffee ground. *Environ. Pollut.* **2017**, *229*, 942–949. [CrossRef]
33. Mahmoud, D.K.; Salleh, M.A.M.; Karim, W.A.; Idris, A.; Abidin, Z.Z. Batch adsorption of basic dye using acid treated kenaf fibre char: Equilibrium, kinetic and thermodynamic studies. *Chem. Eng. J.* **2012**, *181*, 449–457. [CrossRef]
34. Xue, L.; Gao, B.; Wan, Y.; Fang, J.N.; Wang, S.S.; Li, Y.C.; Muñoz-Carpena, R.; Yang, L.Z. High efficiency and selectivity of MgFe-LDH modified wheat-straw biochar in the removal of nitrate from aqueous solutions. *J. Taiwan Inst. Chem. Eng.* **2016**, *63*, 312–317. [CrossRef]
35. You, H.; Zhang, Y.; Li, W.; Li, Y.; Ma, Y.; Feng, X. Removal of NO_3-N in alkaline rare earth industry effluent using modified coconut shell biochar. *Water Sci. Technol.* **2019**, *80*, 784–793. [CrossRef] [PubMed]
36. Ding, D.; Zhao, Y.; Yang, S.; Shi, W.; Zhang, Z.; Lei, Z.; Yang, Y. Adsorption of cesium from aqueous solution using agricultural residue-walnut shell: Equilibrium, kinetic and thermodynamic modeling studies. *Water Res.* **2013**, *47*, 2563–2571. [CrossRef]
37. Usman, A.R.A.; Sallam, A.S.; Al-Omran, A.; El-Naggar, A.H.; Alenazi, K.K.H.; Nadee, M.; Al-Wabel, M.I. Chemically Modified Biochar Produced from Conocarpus Wastes: An Efficient Sorbent for Fe(II) Removal from Acidic Aqueous Solutions. *Adsorpt. Sci. Technol.* **2013**, *31*, 625–640. [CrossRef]

38. Tan, I.A.W.; Hameed, B.H.; Ahmad, A.L. Equilibrium and kinetic studies on basic dye adsorption by oil palm fibre activated carbon. *Chem. Eng. J.* **2007**, *127*, 111–119. [CrossRef]
39. Wu, Q.; Xian, Y.; He, Z.; Zhang, Q.; Wu, J.; Yang, G.; Zhang, X.; Qi, H.; Ma, J.; Xiao, Y.; et al. Adsorption characteristics of Pb(II) using biochar derived from spent mushroom substrate. *Sci. Rep.* **2019**, *9*, 15999. [CrossRef]
40. Lu, N.; Oza, S. Thermal stability and thermo-mechanical properties of hemp-high density polyethylene composites: Effect of two different chemical modifications. *Compos. Part B Eng.* **2013**, *44*, 484–490. [CrossRef]
41. Tofifighy, M.; Mohammadi, T. Nitrate removal from water using functionalized carbon nanotube sheets. *Chem. Eng. Res. Des.* **2012**, *90*, 1815–1822. [CrossRef]
42. Li, Q.; Wu, J.; Hua, M.; Zhang, G.; Li, W.; Shuang, C.; Li, A. Preparation of permanent magnetic resin crosslinking by diallyl itaconate and its adsorptive and anti-fouling behaviors for humic acid removal. *Sci. Rep.* **2017**, *7*, 17103. [CrossRef]
43. Jin, Z.H.; Wang, B.D.; Ma, L.; Fu, P.B.; Xie, L.L.; Jiang, X.; Jiang, W.J. Air pre-oxidation induced high yield N-doped porous biochar for improving toluene adsorption. *Chem. Eng. J.* **2020**, *385*, 9. [CrossRef]
44. Lyu, H.; Tang, J.; Huang, Y.; Gai, L.; Zeng, E.Y.; Liber, K.; Gong, Y. Removal of hexavalent chromium from aqueous solutions by a novel biochar supported nanoscale iron sulfifide composite. *Chem. Eng. J.* **2017**, *322*, 516–524. [CrossRef]
45. Ray, J.R.; Lee, B.; Baltrusaitis, J.; Jun, Y.-S. Formation of iron(III) (hydr)oxides on polyaspartate and alginate-coated substrates: Effects of coating hydrophilicity and functional group. *Environ. Sci. Technol.* **2012**, *46*, 13167–13175. [CrossRef] [PubMed]
46. Jiang, B.; Zhang, W.; Yang, J.; Yu, Y.; Bao, T.; Zhou, X. Low-Temperature Oxidation of Catocene and Its Influence on the Mechanical Sensitivities of a Fine-AP/Catocene Mixture. *Propellants Explos. Pyrotech.* **2015**, *40*, 854–859. [CrossRef]
47. Zhang, G.; Qin, L.; Chen, L.; Xu, Z.; Liu, M.; Guo, X. One-pot synthesis of mesoporous anatase-TiO_2(B) mixed-phase nanowires decorated with sulfur and Fe_2O_3 nanoparticles for visible-light photochemical oxidation. *ChemCatChem* **2016**, *8*, 426–433. [CrossRef]
48. Streat, M.; Hellgardt, K.; Newton, N.L.R. Hydrous ferric oxide as an adsorbent in water treatment: Part 1. Preparation and physical characterization. *Process Saf. Environ. Prot.* **2008**, *86*, 1–9. [CrossRef]
49. Godlewska, P.; Bogusz, A.; Dobrzyńska, J.; Dobrowolski, R.; Oleszczuk, P. Engineered biochar modified with iron as a new adsorbent for treatment of water contaminated by selenium. *J. Saudi Chem. Soc.* **2020**, *24*, 824–834. [CrossRef]
50. Li, H.B.; Dong, X.L.; da Silva, E.B.; de Oliveira, L.M.; Chen, Y.S.; Ma, L.N.Q. Mechanisms of metal sorption by biochars: Biochar characteristics and modifications. *Chemosphere* **2017**, *178*, 466–478. [CrossRef]
51. Sun, Y.; Zheng, W.S. Polyethylenimine-functioalized polyacrylonitrile anion exchange fiber as a novel adsorbent for rapid removal of nitrate from wastewater. *Chemosphere* **2020**, *258*, 127373. [CrossRef]